# The role of open-volume defects in the annihilation of antisites in a B2-ordered alloy

Ehrler, J.; Liedke, M. O.; Cizek, J.; Boucher, R.; Butterling, M.; Zhou, S.; Böttger, R.; Hirschmann, E.; Trinh, T. T.; Wagner, A.; Lindner, J.; Fassbender, J.; Leyens, C.; Potzger, K.; Bali, R.;

Originally published:

June 2019

**Acta Materialia 176(2019), 167-176**

DOI: https://doi.org/10.1016/j.actamat.2019.06.037

Perma-Link to Publication Repository of HZDR:

https://www.hzdr.de/publications/Publ-28092

# The role of open-volume defects in the annihilation of antisites in a B2-ordered alloy

Jonathan Ehrler[a,b], Maciej Oskar Liedke[c,2], Jakub Čížek[d], Richard Boucher[b], Maik Butterling[c], Shengqiang Zhou[a], Roman Böttger[a], Eric Hirschmann[c], Thu Trang Trinh[c,b], Andreas Wagner[c], Jürgen Lindner[a], Jürgen Fassbender[a], Christoph Leyens[b], Kay Potzger[a], Rantej Bali[a,1]

[a] *Institute of Ion Beam Physics and Materials Research, Helmholtz-Zentrum Dresden-Rossendorf, Bautzner Landstrasse 400, 01328 Dresden, Germany*
[b] *Technische Universität Dresden, Helmholtzstrasse 10, 01069 Dresden, Germany*
[c] *Institute of Radiation Physics, Helmholtz-Zentrum Dresden-Rossendorf, Bautzner Landstrasse 400, 01328 Dresden, Germany*
[d] *Faculty of Mathematics and Physics, Charles University in Prague, V Holešovičkách 2, 18000 Praha 8, Czech Republic*

**Abstract**

The atomic arrangement in certain B2-ordered alloys, such as $Fe_{60}Al_{40}$, determines intrinsic material properties like magnetism. Here we have investigated the influence of open-volume defects on the atomic ordering process at elevated temperatures in $Fe_{60}Al_{40}$ thin films. A dependence of the ordering process on the type and concentration of defects is observed by positron annihilation spectroscopy combined with *ab-initio* calculations. Comparing the lifetimes of positrons in the alloy for different annealing and irradiation treatments reveals the role of mono-vacancies, triple defects as well as large vacancy clusters: The rate of atomic ordering to the ordered B2 state is increased in the presence of mono-vacancies whereas triple defects and vacancy complexes decrease the ordering rate. Furthermore, an agglomeration of vacancies during annealing to di-vacancies and larger vacancy clusters is observed. The distribution of open-volume defects can be modified in such a way as to control the thermal stability *via* ion-irradiation and thermal pre-treatments.

*Keywords:* Order-disorder phenomena, Vacancies, Lattice defects, Reordering, Positron Annihilation Spectroscopy

## 1. Introduction

Vacancies are a common type of defects in alloy systems occurring in a variety of forms, from single atomic mono-vacancies to much larger agglomerations of vacancies, called vacancy complexes or clusters. The distribution of open-volume defects can determine application relevant parameters, such as the temperature for thermal annealing [1, 2, 3, 4], *i.e.* even when vacancies may not be directly correlated with the functional property of an alloy, they can profoundly influence the process path to achieve desirable properties. Open-volume defects in $Fe_{60}Al_{40}$ alloy thin films are typically high in concentration [5, 6, 7]. From literature, ordered $Fe_{60}Al_{40}$ is known to possess mono-vacancies as well as triple defects [8, 9] (Figure 1).

However, the role of the above vacancies on the ordering is unclear so far. The $Fe_{60}Al_{40}$ alloy can be ordered to the B2 structure by a thermal treatment, and *via* introducing antisite defects, it is gradually disordered to the A2 structure. The degree of A2/B2 ordering is strongly correlated to its saturation magnetization ($M_s$), which is an intrinsic property. The chemically disordered A2 phase is ferromagnetic and atomic ordering reduces $M_s$ until the paramagnetic B2 phase is achieved [7, 10, 11, 12, 13, 14, 15, 16, 17, 18, 19, 20, 21]. Magnetization measurements therefore allow for a quick and reliable estimate of the alloy ordering. Moreover, irradiation with light noble gas ions, such as $Ne^+$, can deterministically induce antisite defects.

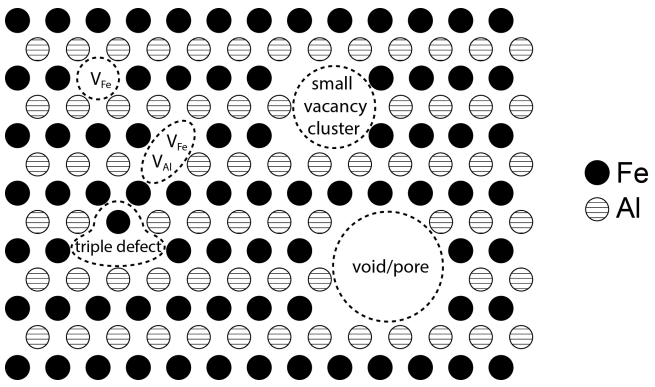


Figure 1: Schematic of various defects in an ordered B2 lattice.

The open-volume defect distribution is measured using positron annihilation spectroscopy (PAS), which allows for determining the defect size (type) and its atomic surrounding in a non-destructive manner. Figure 1 shows a schematic of a B2-ordered Fe-Al alloy with several defect types discussed in this work: If two mono-vacancies ($V_{Fe}$

[1] r.bali@hzdr.de
[2] m.liedke@hzdr.de

and/or $V_{Al}$) couple, a di-vacancy is formed (*e.g.* $V_{Fe}$+$V_{Al}$). The combination of two Fe vacancies with an Fe antisite atom is called triple defect. Vacancy clusters are large agglomerations of vacancies; if the diameter of these clusters exceeds 0.4 nm they are called voids or (micro-)pores [22].

The variation of magnetic and structural properties during the A2 → B2 ordering process at elevated temperatures has been reported recently [7, 12, 13, 23, 24, 25, 26]. Differential scanning calorimetry (DSC) measurements revealed chemical ordering at 400-440 K and grain growth at 680 K [12, 25, 26]. No change of the open-volume defect concentration during the ordering process has been observed in the case of $Fe_{60}Al_{40}$ films, likely due to a much lower initial disordering level of the as-grown films [7]. However, different defect types are expected to impact the ordering due to the relevance of vacancies in the diffusion process.

In this study we aim to directly observe the open-volume defects distribution and sizes. Moreover, we show that the atomic ordering of initially disordered $Fe_{60}Al_{40}$ thin films strongly depends on the defect types and their respective concentrations. The defects can be engineered by a thermal pre-treatment and/or ion-irradiation offering a control of the subsequent A2 → B2 ordering process.

## 2. Experimental

Polycrystalline $Fe_{60}Al_{40}$ thin films with a thickness of 250 nm were prepared by single-target magnetron-sputtering on Si(001) substrates with a ≈250 nm $SiO_2$ buffer layer. These 'as-grown' films consist of a mixture of the B2 and A2 structural phase. The chemically ordered, paramagnetic B2 phase was generated by annealing the as-grown films for 1 hr at 773 K. The fully disordered A2 phase, on the other hand, was generated by ion-irradiation of the as-grown film with $Ne^+$ at an energy of 170 keV and a fluence of $6{\cdot}10^{14}$ ions/cm$^2$; in the following denoted as 'as-grown(irr)'. Alternatively, the A2 phase was generated by ion-irradiation of the B2 film leading to the 'B2(irr)' sample state. The ion energy was selected based on Monte-Carlo type simulations implementing the binary collision approximation [27] to disorder the whole film volume by positioning the peak of the quasi-Gaussian profile in half-depth. The selected ion fluence is known to induce the nominally fully disordered A2 phase in $Fe_{60}Al_{40}$ thin films [18]. The sample denotations and their respective preparations are summarized in Table 1. These initial sample states were ordered *via* annealing at ≈400 K, except for the B2 film which is already fully ordered. That way post-annealed as-grown, as-grown(irr), and B2(irr) films will be referred as such in the further text.

The magnetic characterization was performed by SQUID-VSM (Superconducting Quantum Interference Device vibrating sample magnetometry). The magnetization, M, was measured in saturation by applying 1.2 T during the post-annealing process. The heating and cooling rates were set to 5 K/min. Two different annealing procedures have been applied: First, isochronal annealing from 373 K to 773 K in steps of 50 K, where the temperature was kept constant for 10 min at each step. Second, an isothermal annealing at 400 K for 1 hr. The saturation magnetization ($M_s$) was obtained from hysteresis curves measured between ±1.2 T at 300±0.5 K before and after the annealing process.

The defects were characterized by two different positron annihilation spectroscopy techniques: Doppler broadening spectroscopy (DBS) and positron annihilation lifetime spectroscopy (PALS). The mean positron penetration depth ($z_{mean}$ in units of nm) depends on the positron implantation energy ($E_p$ in units of keV) and is obtained from Makhov profiles [28], which are calculated from Monte-Carlo simulations, and can be approximated by the empirical formula $z_{mean} = 6.11 \cdot E_p^{1.62}$ [7]. The positron energy was set to 5 keV, which corresponds to a penetration depth close to half-depth of the thin films. The DBS measurements were performed at room temperature before and after thermal annealing at 400 K, without breaking the vacuum.

In general, positrons implanted into a solid thermalize after short time (about 10 ps) and diffuse. They localize mostly in open-volume defects, where they annihilate with electrons emitting usually 2 gamma photons as

Table 1: Description of the different denoted $Fe_{60}Al_{40}$ thin films showing the preparation of the initial states and the post treatment.

| Sample denotation | Preparation | Initial $M_s$ in kA/m | Crystal Structure | $M_s$ after post-annealing in kA/m |
|---|---|---|---|---|
| as-grown | 250 nm sputtered film | 224 | B2/A2 mixture | 162 |
| as-grown(irr) | irradiation of an as-grown film with $6{\cdot}10^{14}$ $Ne^+$/cm$^2$ at 170 keV | 518 | A2 | 200 |
| B2 | annealing of an as-grown film at 773 K for 1 hr | 13 | B2 | |
| B2(irr) | irradiation of a B2 film with $6{\cdot}10^{14}$ $Ne^+$/cm$^2$ at 170 keV | 444 | A2 | 64 |

a consequence. Since positrons at their annihilation site have very small momentum compared to the electrons, the broadening of the 511 keV line is observed is mostly due to momentum of the electrons. The annihilation gammas are measured with one or two high-purity Ge detectors (energy resolution better than 1.1 keV at 511 keV). This broadening is characterized by two distinct parameters, namely S and W, defined as a fraction of the annihilation line in the middle and outer regions, respectively. Depth dependent information are provided by plotting the calculated S- and W-parameter as a function of positron implantation energy, S(E) and W(E). The S-W plots, on the other hand, are used to examine the annihilation site and its atomic surrounding [29].

To obtain additional information about the defects, PALS was performed before, during, and after annealing for 1 hr at 423 K. The heating rate was ∼20 K/min and the spectra were recorded at temperatures between 303 K and 423 K in steps of 20 K with statistics of 5 million counts per spectrum. During annealing at 423 K, the spectra were measured continuously with about 5 min per spectrum, which corresponds to approximately 10 million counts per spectrum. The positron annihilation lifetime distributions have been analyzed using the PALSfit [30] program taking the experimental timing resolution into account. The decomposition of the lifetime distribution into characteristic components allows for identification and quantification of defects and defect concentrations due to the sensitivity on the local electron density. The DBS and PALS measurements were performed at the AIDA setup [7] and the MePS beamline, respectively, at the ELBE (Electron Linac for beams with high Brilliance and low Emittance) facility at the Helmholtz-Zentrum Dresden-Rossendorf. More details about the setups can be found in Ref. 31.

## 3. *Ab-initio* calculations of positron lifetimes

Positron lifetimes for the delocalized state (bulk lifetime) and the trapped state at various defects were obtained using the density functional theory (DFT) *ab-initio* calculations within the so-called standard scheme [32]. In this approximation, the positron density is assumed to be everywhere vanishingly small and not affecting the bulk electron structure. In the calculations, at first the electron density in the material is solved without considering the positrons. Subsequently, the positron density is calculated by solving a single particle Schrödinger equation for the positron in an effective potential produced by the electrons and nuclei. The positron lifetime is then calculated from the overlap of the positron and electron density [32]. The electron-positron correlation was treated within the local density approximation using the parametrization derived by Boronski and Nieminen [33].

*Ab-initio* calculations were performed for the disordered A2 and the ordered B2 structure using the lattice parameter $a_0 = 2.896$ Å[34]. The point defects were modeled using a 128 atom based supercell. A Brillouin-zone integration over the lowest-lying positron state, described in Ref. 35, was used in the calculations of the positron parameters for point defects to achieve a rapid convergence of the results with respect to the supercell size. The A2 disordered phase was modeled by random filling of the lattice sites of the supercell with Fe and Al ions in the concentration corresponding to the composition $Fe_{60}Al_{40}$. Positron lifetime calculations were performed for 10 randomly generated A2 supercells and the results were statistically evaluated.

## 4. Results

Figure 2a shows the decay of the magnetization during isochronal annealing from 373 K to 773 K for the three initial sample states, *i.e.* as-grown, as-grown(irr), and B2(irr). The decay of the magnetization and hence the degree of atomic ordering differs significantly among the initial states of the films; the fully ordered B2 phase (M=0) is achieved at different temperatures. Previously, the onset of ordering was observed at ∼400 K [12, 25, 26]. The isothermal annealing at 400 K for 1 hr reveals three different decay rates for the three different initial states, as seen in Figure 2b.

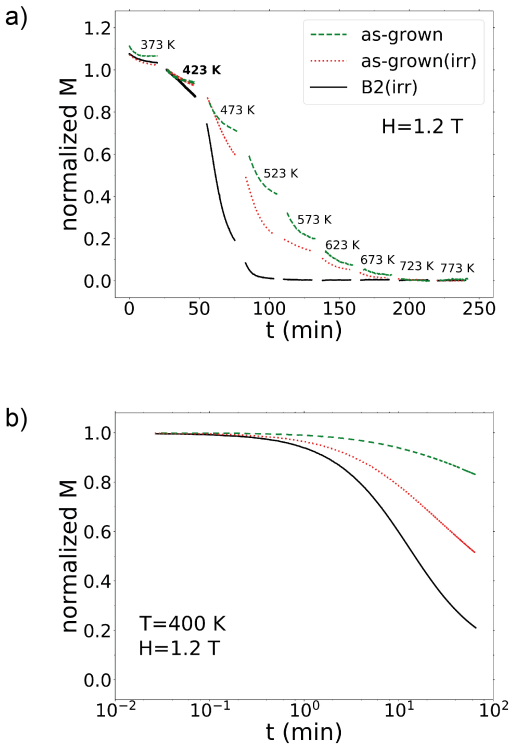


Figure 2: De-magnetization (M) over time during annealing **(a)** in 50 K steps from 373 K to 773 K with 10 min per step and **(b)** at 400 K for 60 min; for the three initial sample states: (Black line) B2(irr), (Dotted red line) as-grown(irr), (Dashed green line) as-grown.

The room temperature saturation magnetization ($M_s$) of both fully disordered A2 films, *i.e.* as-grown(irr) and B2(irr), decreases from initially 518 kA/m and 444 kA/m to 200 kA/m and 64 kA/m, respectively, upon annealing for 1 hr at 400 K. The $M_s$ of the as-grown film, which consists of a mixture of B2 and A2, decreases much less from 224 kA/m to 162 kA/m (supplement, Figure 6). Hence, the atomic ordering results in a drop in $M_s$ of 28 %, 61 %, and 86 % for the as-grown, as-grown(irr), and B2(irr) films, respectively. $Ne^+$ irradiation of as-grown films increased the ordering rate during the subsequent annealing even though more disorder is induced as compared to the as-grown state.

For the identification of the microscopic mechanism leading to such drastic differences in the annealing behavior, PAS has been utilized. Figure 3 shows the relation between the two line shape parameters, S and W, before and after annealing, which were obtained from DBS measurements using a positron implantation energy of $E_p$=5 keV. The energy dependency of S and W can be found in the supplementary material (Figure 7). The $Ne^+$ irradiated films as well as the fully ordered B2 film are located on a straight line, which goes upon extrapolation through the defect-free Fe bulk reference value. The annealing of the irradiated samples moves the S-W values in direction of the Al bulk reference value, however, still located on the same line. In contrast to both irradiated films, the S-W values of the as-grown films, before and after annealing, are not located on this straight line.

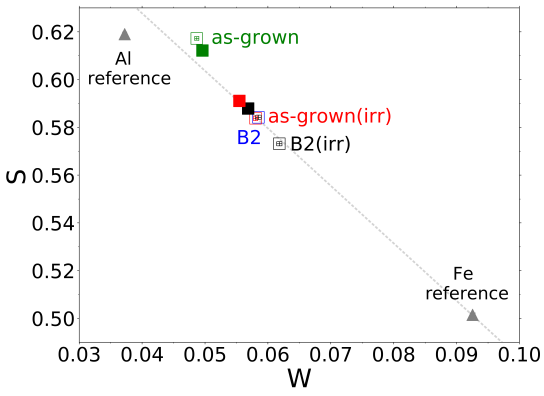


Figure 3: Relation between the two line shape parameters, S and W, obtained from DBS measurements for a positron implantation energy of $E_p$=5 keV. The initial sample states (empty squares) are labeled next to the data points and the filled squares indicate the post-annealing at 400 K.

Besides DBS, another method to characterize open-volume defects with respect to their size distribution is the determination of positron lifetime. Figure 4a shows distinct values for positron lifetimes associated with distinct types of open-volume defects for the three initial sample states, *i.e.* as-grown, as-grown(irr), and B2(irr). For comparison, the positron lifetime distribution for the B2-ordered film is shown in Figure 4a as well. The positron lifetime distribution for the post-annealed samples is shown in Figure 4b. The data can be found in the supplement in Table 3. The positron lifetime values and the respective intensities of the annihilation lines have additionally been measured in-situ, i.e. during the annealing process. These show a monotonic behavior (supplement, Figures 8a-d). The shortest positron lifetime varies for all sample states, before as well as after annealing, slightly in the range between 184-207 ps (Figures 4a and b). For the as-grown film, three positron lifetimes are observed. The annealing of the as-grown film at 773 K leads to the formation of the B2 phase and the occurrence of a fourth lifetime above 20 ns; the second lifetime decreases significantly from 490 ps to 288 ps. After $Ne^+$ irradiation of the as-grown and B2 films, only two positron lifetimes below 500 ps are observed. The ion-irradiation of as-grown films reduces the second lifetime from 490 ps to 414 ps whereas in the case of the B2 film no change is observed. The post-annealing at 423 K induces only a slight variation of the shortest positron lifetimes as well as the ones above 1 ns; the lifetimes in the range between 250-500 ps decrease upon annealing for all sample states.

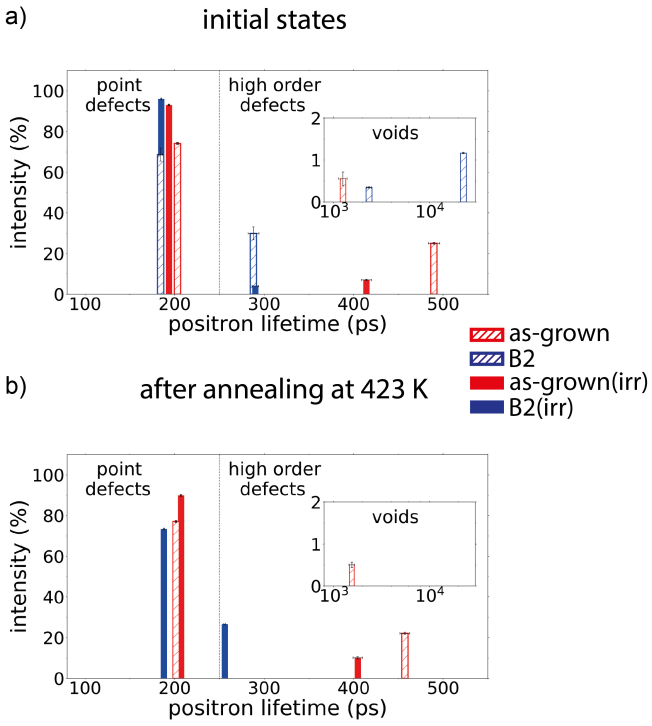


Figure 4: Positron lifetimes and their respective intensities obtained by fitting the PALS measurements using PALSfit [30] **(a)** before and **(b)** after annealing at 423 K for the different sample states given in the legend. The inset shows the respective positron lifetimes above 1 ns. The positron implantation energy was set to 5 keV.

## 5. Simulations and Discussion

The positron lifetimes in the ps-regime, observed in all films, refer to point defects like mono-vacancies and triple defects [8, 36] and defects of higher order, *e.g.* surfaces and small vacancy clusters located within the grains or at grain boundaries [37, 38]. The positron lifetimes above ∼1 ns, observed in the non-irradiated films, result from the pick-off annihilation of ortho-positronium formed in voids or pores, *i.e.* vacancy clusters larger than 0.4 nm [22, 39, 40]. In order to identify the respective defect types and their impact on the ordering process, *ab-initio* calculations of positron lifetimes were performed. The calculated positron lifetimes for different defect configurations in B2-$Fe_{60}Al_{40}$ can be found in the supplement in Table 2. However, the lifetime of positrons trapped in an open-volume defect depends not only on its open-volume but also on the atomic surrounding; hence, antisite disorder causes a certain spread of the calculated lifetimes. For example the bulk positron lifetime for fully disordered (A2 structure) $Fe_{60}Al_{40}$ varies from 106 ps to 114 ps, depending on the local variations of chemical composition. These variations are even larger for positrons localized at defects. The lifetime of positrons trapped in mono-vacancies in A2-$Fe_{60}Al_{40}$ increases linearly with an increasing number of Al nearest neighbors (supplement, Figure 9).

The S-W values of the $Ne^+$ irradiated films as well as the one of the ordered B2 film are located on a straight line going through the Fe bulk reference value (Figure 3) implying that defects located in the Fe sublattice are the dominant annihilation sites; Fe vacancies are known to possess a lower formation energy than Al vacancies in Fe-Al alloys [41, 42, 43]; however, ion-irradiation induces Fe as well as Al mono-vacancies. The off-line position of the as-grown films indicates the positron annihilation in a different type of defects. The post-annealing of the irradiated samples changes the defect decoration promoting Al surrounding since the S-W values move in direction of the Al bulk reference value, however, the annihilation still occurs in defects in the Fe sublattice. An increasing Al surrounding of the defects in the Fe sublattice indicates an increase of chemical order (B2), which is in agreement with the decreasing $M_s$ (Figure 2b). A larger number of Al nearest neighbors increases the positron lifetime, as obtained from *ab-initio* calculations.

Figure 5 shows the obtained positron lifetimes below 300 ps for the different sample states. The calculated positron lifetime regimes for various defect types, *i.e.* mono-vacancies, di-vacancies, triple defects, and small intragranular defect clusters are shaded grey; the ranges are calculated for the respective defects surrounded by Fe or Al nearest neighbors only. In the present study, no positron annihilation in defect-free bulk is observed due to the high vacancy concentration in the $Fe_{60}Al_{40}$ thin films.

The positron lifetime of the high order defects in the as-grown film (490 ps) is much higher than the ones calculated for mono-vacancies or small intragranular vacancy clusters (supplement, Table 2); hence, this lifetime refers to positrons trapped in large vacancy clusters or nano-voids located at triple points, *i.e.* intersection of three or more grain boundaries [44]. The calculations reveal the type of point defects in as-grown films with a lifetime of 203 ps as triple defects (Figure 5). Triple defects consist of 2 Fe vacancies and 1 Fe antisite atom and are known to be stable in Fe-Al alloys [42, 45, 46]. Hence, triple defects imply antisite disorder explaining the ferromagnetism in as-grown films. The ordering to the B2 structure *via* annealing the as-grown film at 773 K decreases the positron lifetime in the high order defect regime strongly from 490 ps to 288 ps (Figure 4a). The lifetimes between 250 ps and 300 ps refer to intragranular vacancy clusters consisting of ≥5 vacancies, as obtained from the simulations, implying an agglomeration of vacancies during the annealing process (Figure 5). The low concentration of voids is still present after annealing. The triple defects present in the as-grown films transform into mono-vacancies (lifetime ≤190 ps). A transformation of triple defects is reasonable since they require an Fe antisite atom and B2-$Fe_{60}Al_{40}$ is characterized by a minimum of antisite disorder.

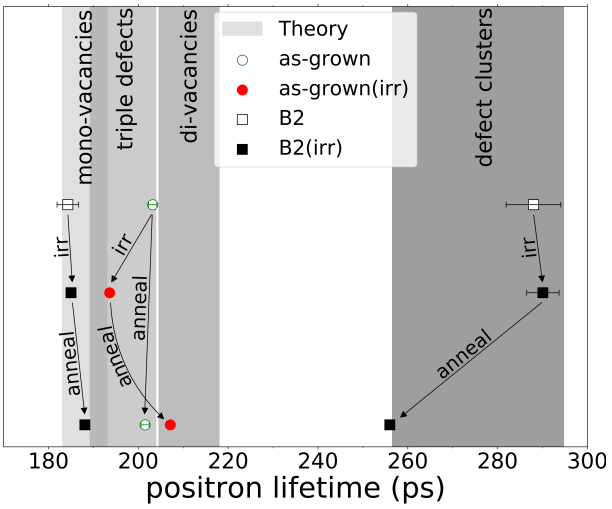


Figure 5: Obtained positron lifetimes at an implantation energy of $E_p$=5 keV for the initial sample states and after annealing at 423 K, except for the large vacancy clusters. The respective sample states are described in the legend. The positron lifetime regimes for various defect types, as obtained from *ab-initio* calculations, are shaded grey.

$Ne^+$ irradiation of the as-grown film decreases the lifetime (size) and the intensity (concentration) of the large vacancy clusters located at triple points significantly; in addition, no voids or pores are observed in the as-grown(irr) film indicating a fragmentation of the vacancy clusters into smaller open-volume defects due to $Ne^+$ irradiation (Figure 4a). The as-grown(irr) film contains defects with an intermediate lifetime of 194 ps located in the regime where mono-vacancies and triple defects occur (Figure 5). Ion-irradiation is known to induce vacancies distributed

randomly in both, Fe and Al, sublattices. Similarly, the B2-ordered film has been ion-irradiated; here, likewise no voids or pores are observed and the concentration of the intragranular vacancy clusters with a positron lifetime ∼290 ps decreases significantly from 30 % to 4 % indicating a fragmentation of vacancy clusters. The concentration of mono-vacancies, on the other hand, increases from 69 % to 96 % (Figure 4a).

Among the initial sample states, the as-grown film shows the smallest drop in $M_s$ (28 %) upon isothermal post-annealing at 423 K (Figure 2b) indicating the lowest degree of atomic ordering. The triple defects and vacancy clusters are found to be stable at 423 K decreasing the atomic ordering *via* vacancies (Figures 4b and 5). The ordering rate within the as-grown(irr) film during post-annealing is strongly increased as compared to the non-irradiated film indicated by an increasing drop in $M_s$ from 28 % to 61 % (Figure 2b), which results from the ion-irradiation induced fragmentation of the vacancy clusters as well as the creation of randomly distributed mono-vacancies. The observed mixture of mono-vacancies and triple defects in the as-grown(irr) film with a positron lifetime of 194 ps changes upon post-annealing to 207 ps. Since $M_s$ decreases strongly during annealing (Figure 2b) a formation of triple defects, implying antisite disorder, is unlikely to occur. The increased lifetime of 207 ps refers to di-vacancies (Figure 5), which implies an agglomeration of mono-vacancies as well as a transformation of triple defects during post-annealing. Since triple defects are found to be stable during post-annealing of the as-grown film, a mono-vacancy assisted triple defect transformation is assumed. The post-annealing of the B2(irr) film confirms the above observations: The predominant amount of mono-vacancies (96 %) as well as the fragmentation of vacancy clusters (Figure 4a) increase the ordering rate significantly indicated by a drop in $M_s$ of 86 %. The effect of vacancy agglomeration during annealing is also observed for the post-annealing of the B2(irr) film; the concentration of vacancy clusters increases significantly on the expense of mono-vacancies whereas the size of the defect clusters decreases indicating a decomposition of vacancy clusters into smaller ones (Figures 4 and 5).

In summary, Fe and Al mono-vacancies introduced by $Ne^+$ irradiation increase the A2 → B2 ordering rate whereas triple defects and vacancy clusters are stable during annealing at 423 K decreasing the ordering rate.

## 6. Conclusions

The A2 → B2 ordering process in $Fe_{60}Al_{40}$ thin films at elevated temperatures can be controlled by engineering the open-volume defects. The ordering rate is increased by mono-vacancies and decreased by triple defects and vacancy clusters. $Ne^+$ irradiation increases the number of mono-vacancies and leads to a fragmentation of vacancy clusters and hence increases the rate of subsequent atomic ordering by lowering its threshold energy. The number of triple defects decreases strongly by pre-annealing at 773 K. However, a large variety of defect types and concentrations – which would increase or decrease the ordering rate – might be achieved by varying the conditions of film growth, pre-annealing (temperature and time), and ion-irradiation (ion species) as well as their respective combinations. For instance, depending on the ion species, ion-irradiation can induce or stabilize large vacancy clusters [47] or lead to their fragmentation or shrinkage [48, 49, 50]. Besides a control of the thermal stability, a sensitive defect engineering has potential to manipulate further material properties like the electrical conductivity.


## Acknowledgment

The authors thank the team of the Ion Beam Center at the Helmholtz-Zentrum Dresden - Rossendorf for performing the ion irradiations. Positron annihilation lifetime studies were carried out at the ELBE instrument at the Helmholtz-Zentrum Dresden-Rossendorf (POS18101156).

This work was supported by the German Science Foundation (DFG) [BA 5656/1-1], the Federal Ministry of Education and Research (BMBF) [05K2013], and the Czech Science Foundation [P108/12/
G043].



[1] S. Kang, J. W. Harrell, D. E. Nikles, Reduction of the fcc to l10ordering temperature for self-assembled FePt nanoparticles containing ag, Nano Lett. 2 (10) (2002) 1033–1036. doi:10.1021/nl025614b.

[2] L. C. Varanda, M. Jafelicci, Self-assembled FePt nanocrystals with large coercivity: Reduction of the fcc-to-l10ordering temperature, J. Am. Chem. Soc. 128 (34) (2006) 11062–11066. doi:10.1021/ja060711i.

[3] C.-H. Lai, C.-H. Yang, C. C. Chiang, Ion-irradiation-induced direct ordering of l10 FePt phase, Appl. Phys. Lett. 83 (22) (2003) 4550–4552. doi:10.1063/1.1631391.

[4] U. Wiedwald, A. Klimmer, B. Kern, L. Han, H.-G. Boyen, P. Ziemann, K. Fauth, Lowering of the l10 ordering temperature of FePt nanoparticles by $he^+$ ion irradiation, Appl. Phys. Lett. 90 (6) (2007) 062508. doi:10.1063/1.2472177.

[5] M. Jabłońska, A. Hanc, A. Szostak, A study of point defects in the b2-phase region of the fe–al system by mssbauer spectroscopy, Solid State Phenom. 163 (2010) 299–302. doi:10.4028/www.scientific.net/ssp.163.299.

[6] F. Lukč, J. Čižek, I. Prochzka, D. Jirskov, W. Anwand, G. Brauer, Vacancy-induced hardening in fe-al and alloys, J. Phys. Conf. Ser. 443 (2013) 012025. doi:10.1088/1742-6596/443/1/012025.

[7] M. O. Liedke, W. Anwand, R. Bali, S. Cornelius, M. Butterling, T. Trinh, A. Wagner, S. Salamon, D. Walecki, A. Smekhova, H. Wende, K. Potzger, Open volume defects and magnetic phase transition in fe60al40 transition metal aluminide, J. Appl. Phys. 117 (2015) 163908.

[8] J. Wolff, M. Franz, A. Broska, R. Kerl, M. Weinhagen, B. Khler, M. Brauer, F. Faupel, T. Hehenkamp, Point defects and their properties in FeAl and FeSi alloys, Intermetallics 7 (3-4) (1999) 289–300. doi:10.1016/s0966-9795(98)00105-8.

[9] J. Čížek, F. Lukáč, I. Procházka, R. Kužel, Y. Jirásková, D. Janičkovič, W. Anwand, G. Brauer, Characterization of quenched-in vacancies in fe–al alloys, Physica B: Condens. Matter. 407 (14) (2012) 2659–2664. doi:10.1016/j.physb.2011.12.122.

[10] Q. Zeng, I. Baker, Magnetic properties and thermal ordering of mechanically alloyed fe–40at% al, Intermetallics 14 (4) (2006) 396–405. doi:10.1016/j.intermet.2005.07.005.

[11] B. Avar, M. Gogebakan, S. Ozcan, S. Kerli, Structural, mechanical and magnetic properties of fe-40-at.Phys. Soc. 65 (5) (2014) 664–670. doi:10.3938/jkps.65.664.

[12] A. Hernando, X. Amils, J. Nogués, S. Suriñach, M. D. Baró, M. R. Ibarra, Influence of magnetization on the reordering of nanostructured ball-milled fe-40 at. % al powders, Phys. Rev. B 58 (18) (1998) R11864–R11867. doi:10.1103/physrevb.58.r11864.

[13] X. Amils, J. Nogus, S. Surinach, M. D. Bar, J. S. Munoz, Magnetic properties and of ball and milled fe-40a and at.% alloys, IEEE Trans. Magn. 34 (4) (1998) 1129–1131. doi:10.1109/20.706409.

[14] A. J. Bradley, A. H. Jay, The formation of superlattices in alloys of iron and aluminium, Proc. R. Soc., Ser. A 136 (829) (1932) 210–232. doi:10.1098/rspa.1932.0075.

[15] E. Menéndez, J. Sort, M. O. Liedke, J. Fassbender, S. Suriñach, M. D. Baró, J. Nogués, Two-fold origin of the deformation-induced ferromagnetism in bulk fe60al40(at.%) alloys, New J. Phys. 10 (10) (2008) 103030. doi:10.1088/1367-2630/10/10/103030.

[16] P. A. Beck, Some recent results on magnetism in alloys, Metall. Mater. Trans. B 2 (8) (1971) 2015–2024. doi:10.1007/bf02917527.

[17] J. Fassbender, M. O. Liedke, T. Strache, W. Mller, E. Menndez, J. Sort, K. V. Rao, S. C. Deevi, J. Nogus, Ion mass dependence of irradiation-induced local creation of ferromagnetism in $fe_{60}al_{40}$ alloys, Phys. Rev. B 77 (17) (2008) 174430. doi:10.1103/physrevb.77.174430.

[18] R. Bali, S. Wintz, F. Meutzner, R. Hbner, R. Boucher, A. A. nal, S. Valencia, A. Neudert, K. Potzger, J. Bauch, et al., Printing nearly-discrete magnetic patterns using chemical disorder induced ferromagnetism, Nano Lett. 14 (2) (2014) 435–441. doi:10.1021/nl404521c.
URL `http://dx.doi.org/10.1021/nl404521c`

[19] N. Tahir, R. Bali, R. Gieniusz, S. Mamica, J. Gollwitzer, T. Schneider, K. Lenz, K. Potzger, J. Lindner, M. Krawczyk, J. Fassbender, A. Maziewski, Tailoring dynamic magnetic characteristics ofFe60al40films through ion irradiation, Phys. Rev. B 92 (14) (2015) 144429. doi:10.1103/physrevb.92.144429.

[20] F. Rder, G. Hlawacek, S. Wintz, R. Hbner, L. Bischoff, H. Lichte, K. Potzger, J. Lindner, J. Fassbender, R. Bali, Direct depth- and lateral- imaging of nanoscale magnets generated by ion impact, Sci. Rep. 5 (1) (2015) 16786. doi:10.1038/srep16786.

[21] J. Ehrler, M. He, M. V. Shugaev, N. I. Polushkin, S. Wintz, V. Liersch, S. Cornelius, R. Hbner, K. Potzger, J. Lindner, J. Fassbender, A. A. nal, S. Valencia, F. Kronast, L. V. Zhigilei, R. Bali, Laser-rewriteable ferromagnetism at thin-film surfaces, ACS Appl. Mater. Interfaces 10 (17) (2018) 15232–15239. doi:10.1021/acsami.8b01190.

[22] B. Zdravkov, J. Čermák, M. Šefara, J. Janků, Pore classification in the characterization of porous materials: A perspective, Open Chemistry 5 (2). doi:10.2478/s11532-007-0017-9.

[23] M. Fujii, K. Saito, K. Wakayama, M. Kawasaki, T. Yoshioka, T. Isshiki, K. Nishio, M. Shiojir, Ferromagnetism and structural distortions induced in atomized fe-AI (35–42 at.% AI) powder particles by cold milling, Philos. Mag. A 79 (8) (1999) 2013–2023. doi:10.1080/01418619908210406.

[24] S. Gialanella, X. Amils, M. Barò, P. Delcroix, G. L. Car, L. Lutterotti, S. Suriñach, Microstructural and kinetic aspects of the transformations induced in a FeAl alloy by ball-milling and thermal treatments, Acta Mater. 46 (9) (1998) 3305–3316. doi:10.1016/s1359-6454(97)00484-9.

[25] S. Suriñach, X. Amils, S. Gialanella, L. Lutterotti, M. D. Baró, Kinetics of reordering in a nanograined FeAl alloy, Mater. Sci. Forum 235-238 (1997) 415–420. doi:10.4028/www.scientific.net/msf.235-238.415.

[26] C. Mangler, C. Gammer, H. Karnthaler, C. Rentenberger, Structural modifications during heating of bulk nanocrystalline FeAl produced by high-pressure torsion, Acta Mater. 58 (17) (2010) 5631–5638. doi:10.1016/j.actamat.2010.06.036.

[27] J. F. Ziegler, M. Ziegler, J. Biersack, SRIM – the stopping and range of ions in matter (2010), Nucl. Instrum. Methods Phys. Res., Sect. B 268 (11-12) (2010) 1818–1823, http://www.srim.org/SRIM/SRIMLEGL.htm. doi:10.1016/j.nimb.2010.02.091.
URL `http://www.srim.org/SRIM/SRIMLEGL.htm`

[28] A. Makhov, The penetration of electrons into solids, Sov. Phys. Solid State (2) (1961) 2172.

[29] M. Clement, J. M. M. de Nijs, P. Balk, H. Schut, A. van Veen, Analysis of positron beam data by the combined use of the shape- and wing-parameters, J. Appl. Phys. 79 (12) (1996) 9029–9036. doi:10.1063/1.362635.

[30] J. V. Olsen, P. Kirkegaard, N. J. Pedersen, M. Eldrup, PALSfit: A new program for the evaluation of positron lifetime spectra, Phys. Status Solidi C 4 (10) (2007) 4004–4006. doi:10.1002/pssc.200675868.

[31] A. Wagner, M. Butterling, M. O. Liedke, K. Potzger, R. Krause-Rehberg, Positron annihilation lifetime and doppler broadening spectroscopy at the ELBE facility, in: International Workshop on Physics with Positrons at Jefferson Lab, Author(s), 2018. doi:10.1063/1.5040215.

[32] M. J. Puska, R. M. Nieminen, Theory of positrons in solids and on solid surfaces, Rev. Mod. Phys. 66 (3) (1994) 841–897. doi:10.1103/revmodphys.66.841.

[33] E. Boroński, R. M. Nieminen, Electron-positron density-functional theory, Phys. Rev. B 34 (6) (1986) 3820–3831. doi:10.1103/physrevb.34.3820.

[34] A. Taylor, R. Jones, Constitution and magnetic properties of iron-rich iron-aluminum alloys, J. Phys. Chem. Solids 6 (1) (1958) 16–37. doi:10.1016/0022-3697(58)90213-0.

[35] T. Korhonen, M. J. Puska, R. M. Nieminen, First-principles calculation of positron annihilation characteristics at metal vacancies, Phys. Rev. B 54 (21) (1996) 15016–15024. doi:10.1103/physrevb.54.15016.

[36] J. Kansy, H.-K. A., D. Giebel, Change of the defect structure in feal alloy as a result of its aging at ambient temperature, in: PSPA, Vol. 58, 2012, pp. 221–224.

[37] J. Čížek, I. Procházka, M. Cieslar, R. Kužel, J. Kuriplach, F. Chmelík, I. Stulíková, F. Bečvář, O. Melikhova, R. K. Islamgaliev, Thermal stability of ultrafine grained copper, Phys. Rev. B 65 (9). doi:10.1103/physrevb.65.094106.

[38] B. Oberdorfer, R. Wrschum, Positron trapping model for point defects and grain boundaries in polycrystalline materials, Phys. Rev. B 79 (18). doi:10.1103/physrevb.79.184103.

[39] K. Wada, T. Hyodo, A simple shape-free model for pore-size estimation with positron annihilation lifetime spectroscopy, J. Phys. Conf. Ser. 443 (2013) 012003. doi:10.1088/1742-6596/443/1/012003.

[40] A. Zubiaga, F. Tuomisto, M. J. Puska, Pick-off annihilation of positronium in matter using full correlation single particle potentials: Solid he, The Journal of Physical Chemistry B 119 (4) (2015) 1747–1755. doi:10.1021/jp5106295.

[41] M. Eggersmann, H. Mehrer, Diffusion in intermetallic phases of the fe-al system, Philos. Mag. A 80 (5) (2000) 1219–1244. doi:10.1080/01418610008212112.

[42] A. Kellou, H. Feraoun, T. Grosdidier, C. Coddet, H. Aourag, Energetics and electronic properties of vacancies, anti-sites, and atomic defects (b, c, and n) in b2-FeAl alloys, Acta Mater. 52 (11) (2004) 3263–3271. doi:10.1016/j.actamat.2004.03.023.

[43] Y. Ouyang, X. Tong, C. Li, H. Chen, X. Tao, T. Hickel, Y. Du, Thermodynamic and physical properties of FeAl and fe3al: an atomistic study by EAM simulation, Physica B 407 (23) (2012) 4530–4536. doi:10.1016/j.physb.2012.08.025.

[44] H.-E. Schaefer, R. Wrschum, R. Birringer, H. Gleiter, Structure of nanometer-sized polycrystalline iron investigated by positron lifetime spectroscopy, Phys. Rev. B 38 (14) (1988) 9545–9554. doi:10.1103/physrevb.38.9545.

[45] Y. Chang, L. Pike, C. Liu, A. Bilbrey, D. Stone, Correlation of the hardness and vacancy concentration in FeAl, Intermetallics

1 (2) (1993) 107–115. doi:10.1016/0966-9795(93)90028-t.

[46] M. Kogachi, T. Haraguchi, S. Kim, Point defect behavior in high temperature region in the b2-type intermetallic compound FeAl, Intermetallics 6 (6) (1998) 499–510. doi:10.1016/s0966-9795(97)00097-6.

[47] O. El-Atwani, E. Esquivel, M. Efe, E. Aydogan, Y. Wang, E. Martinez, S. Maloy, Loop and void damage during heavy ion irradiation on nanocrystalline and coarse grained tungsten: Microstructure, effect of dpa rate, temperature, and grain size, Acta Mater. 149 (2018) 206–219. doi:10.1016/j.actamat.2018.02.035.

[48] K. C. Russell, Theory of nucleation with cluster loss and injection: Application to plastic deformation and irradiation, Metall. Mater. Trans. A 27 (6) (1996) 1441–1448. doi:10.1007/bf02649805.

[49] Y. Chen, K. Y. Yu, Y. Liu, S. Shao, H. Wang, M. A. Kirk, J. Wang, X. Zhang, Damage-tolerant nanotwinned metals with nanovoids under radiation environments, Nat. Commun. 6 (1). doi:10.1038/ncomms8036.

[50] J. Li, C. Fan, J. Ding, S. Xue, Y. Chen, Q. Li, H. Wang, X. Zhang, In situ heavy ion irradiation studies of nanopore shrinkage and enhanced radiation tolerance of nanoporous au, Sci. Rep. 7 (1). doi:10.1038/srep39484.

## SUPPLEMENT

Figure 6 shows the hysteresis curves measured by vibrating sample magnetometry at 300±0.5 K before and after post-annealing (at 400 K) the thin films, *i.e.* B2(irr), as-grown(irr), and as-grown. Both irradiated films, before any annealing, are nominally fully disordered, however, there is a slight difference in the saturation magnetization ($M_s$).

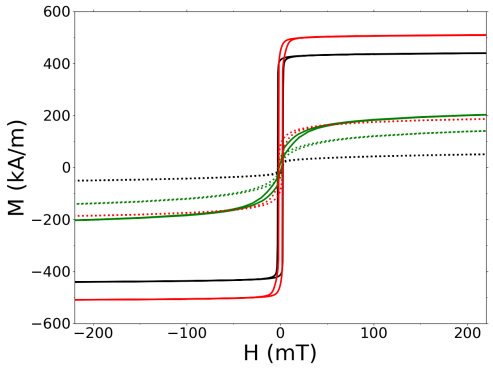


Figure 6: Hysteresis curves before (solid lines) and after (dashed lines) post-annealing at 400 K for the sample states as-grown (green), as-grown(irr) (red), and B2(irr) (black).

Doppler broadening spectroscopy measurements were also performed without breaking the vacuum before and after post-annealing at 400 K. The positron implantation energy ($E_p$) was varied between 0.05 and 35 keV; however, the $Fe_{60}Al_{40}$-$SiO_2$ interface is reached at $E_p \approx 10$ keV. The high S-parameter of the as-grown film indicates a large open-volume defect concentration, which decreases only slightly after annealing at 400 K. The defect concentration decreases strongly after ion-irradiation; the lowest concentration is observed for the B2(irr) film. The open-volume defect concentration increases after annealing for both irradiated films.

Note that the mean positron penetration depth ($z_{mean}$) depends on the density of the alloy, which is related to the chemical order since antisite disorder increases the lattice constant; this implies that $z_{mean}$ can vary slightly for the various films. Here, $z_{mean}$ was calculated for the intermediate density of 5.89 g/cm$^3$.

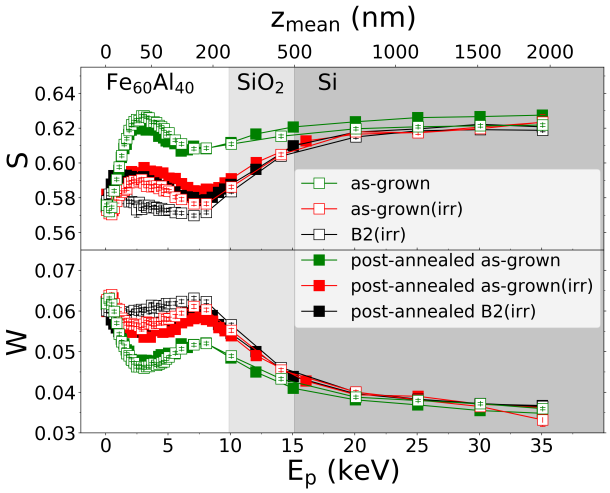


Figure 7: Energy-dependency of the S- and W-parameter before and after post-annealing. The sample states are given in the legend.

The variations of the positron lifetimes and the intensities of the different initial sample states, *i.e.* B2(irr), as-grown(irr), and as-grown, during post-annealing at 423 K are illustrated in Figure 8 showing a monotonic behavior.

The calculated positron lifetimes for various defect types in B2-$Fe_{60}Al_{40}$ are shown in Table 2. The lifetime of positrons trapped in an open-volume defect depends also on the atomic surrounding. Therefore, the dependency of the positron lifetime in a mono-vacancy on the Al nearest neighbors is shown in Figure 9; the lifetime increases linearly with an increasing number of Al nearest neighbors.

The fitting results of the positron annihilation lifetime spectroscopy (PALS) measurements at $E_p$=5 keV for various sample states before and after in-situ annealing at 423 K are presented in Table 3. The data are illustrated graphically in the paper in Figures 4a and b.

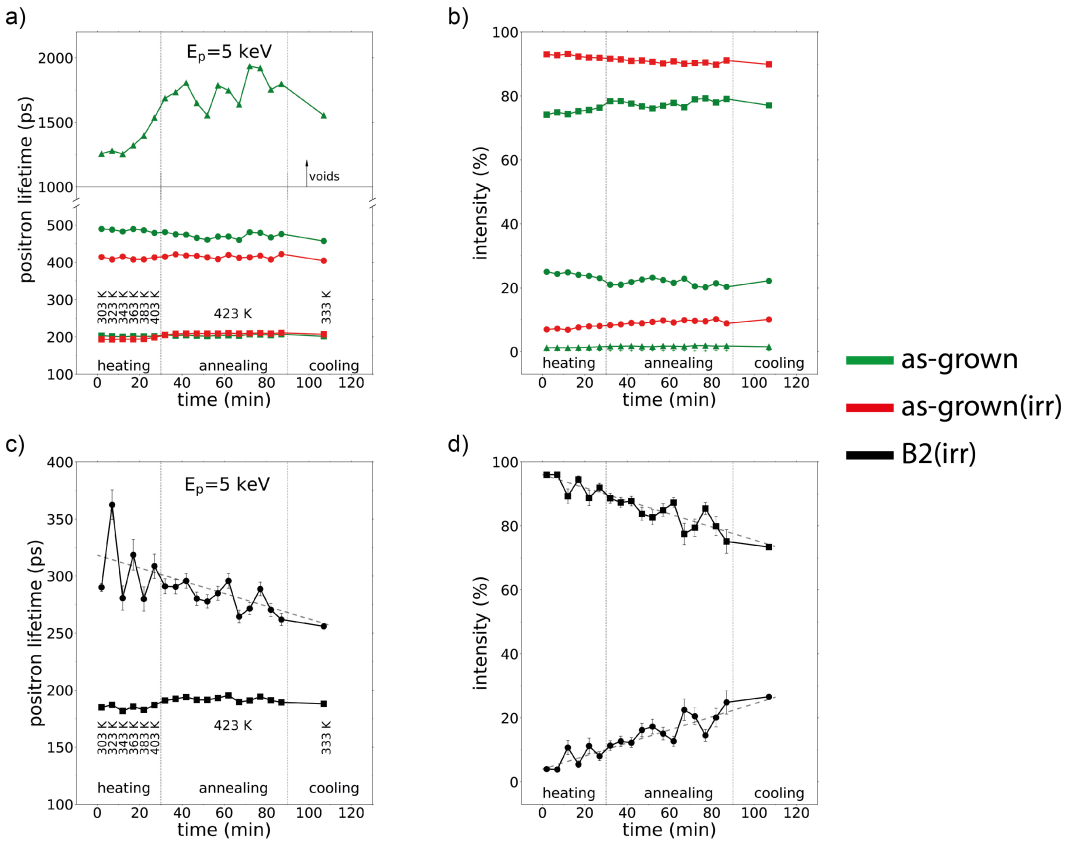


Figure 8: **Variation of the positron lifetimes (a, c) and their respective intensities (b, d) during post-annealing.** (Green) as-grown, (Red) as-grown(irr), (Black) B2(irr). The several lifetimes and their respective intensities are marked with symbols. The dashed lines in c and d serve as a guide to the eye.

Table 2: Calculated positron lifetimes for various defect types in B2-$Fe_{60}Al_{40}$.

| Defect configuration | Lifetime /ps |
|---|---|
| defect-free bulk | 112.6 |
| mono-vacancies | |
| $V_{Fe}$ | 189.9 |
| $V_{Al}$ | 184.0 |
| triple defects | |
| $2V_{Fe}$+$1Fe_{Al}$ (single triple defect) | 198.6 |
| $3V_{Fe}$+$2Fe_{Al}$ (two triple defects) | 201.6 |
| $4V_{Fe}$+$3Fe_{Al}$ (three triple defects) | 203.3 |
| continuous chain of triple defects | ≈204 |
| di-vacancy | |
| $V_{Fe}$+$V_{Al}$ | 210.8 |
| tri-vacancy | |
| $2V_{Fe}$+$V_{Al}$ | 231.6 |
| small vacancy clusters | |
| $4V_{Fe}$+$1V_{Al}$ | 258.8 |
| $4V_{Fe}$+$2V_{Al}$ | 257.8 |
| $8V_{Fe}$+$1V_{Al}$ | 295.7 |

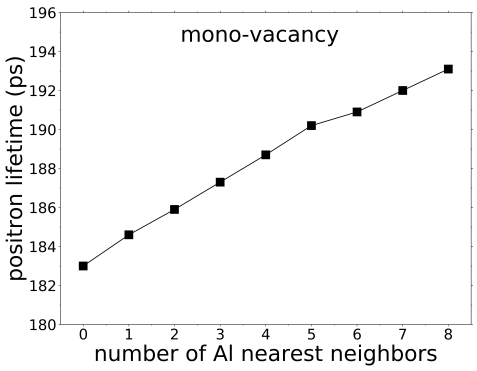


Figure 9: Calculated positron lifetime in mono-vacancies in disordered A2-$Fe_{60}Al_{40}$ depending on the number of Al nearest neighbors.

Table 3: Results of the PALS analysis for an energy of incident positrons $E_p$=5 keV: Intensity and Lifetime of the defects within the various sample states.

| Sample state | Intensity /% and Lifetime /ps | | | |
|---|---|---|---|---|
| initial states | | | | |
| as-grown | 74.2(6)<br>203(1) | 25.0(4)<br>490(6) | 0.6(2)<br>1200(100) | |
| B2 | 69(5)<br>184(2) | 30(3)<br>288(6) | 0.35(1)<br>2300(100) | 1.167(8)<br>22500(200) |
| as-grown(irr) | 93.0(3)<br>194(1) | 7.0(3)<br>414(6) | | |
| B2(irr) | 96.0(5)<br>185(0) | 3.9(5)<br>290(4) | | |
| after annealing at 423 K | | | | |
| post-annealed as-grown | 77.1(6)<br>202(1) | 22.2(5)<br>457(5) | 0.7(1)<br>1500(100) | |
| post-annealed as-grown(irr) | 89.9(5)<br>207(1) | 10.1(5)<br>405(5) | | |
| post-annealed B2(irr) | 73.4(0)<br>188(0) | 26.6(0)<br>256(1) | | |